# Comparative study of wall-shear stress at the ascending aorta for different mechanical heart valve prostheses

**Qianhui Li**[1]
School of Mathematics, Computer Science and Engineering,
City, University of London,
Northampton square, London, EC1V 0HB, UK
Qianhui.li@city.ac.uk

**Franziska Hegner**
Institute of Mechanics and Fluid Dynamics,
Technical University Bergakademie Freiberg,
Freiberg, Germany
Franziska.Hegner@extern.tu-freiberg.de

**Christoph H. Bruecker**
School of Mathematics, Computer Science and Engineering,
City, University of London,
Northampton square, London, EC1V 0HB, UK
Christoph.Bruecker@city.ac.uk

**Abstract**

*An experimental study is reported which investigates the wall shear stress (WSS) distribution in a transparent model of the human aorta comparing an SJM Regent bileaflet mechanical heart valve (BMHV) with the Lapeyre-Triflo FURTIVA trileaflet mechanical heart valve (TMHV) in physiological pulsatile flow. Elastic micro-cantilever structures, calibrated as micro-pillar WSS sensors by micro-Particle-Image-Velocimetry measurements, are applied to the wall along the ascending aorta (AAo). The peak WSS values*

[1] Corresponding author

*in the BMHV are observed to be almost twice that of the values seen in the TMHV. Flow field analysis illuminates that these peaks are linked to the jet-like flows generated in the valves interacting with the aortic wall. Not only the magnitude but also the impact regions are specific for different valve designs. The side-orifice jets generated by the BMHV travel along the aortic wall in the AAo, impacting the wall throughout the AAo. However, the jets generated by TMHV impact further downstream in the AAo and results in a reduced WSS.*

***Keywords:*** *aortic valve flow, PIV, wall shear stress, micro-pillar sensors*

## 1. Introduction

The heart valves of the left ventricle of the human heart are subject to the highest mechanical loads of all valves and therefore are often the first to deteriorate in elderly people [1]. The mitral valve and the aortic valve control the unidirectional flow of oxygenated blood from the lung towards the arterial system via the left ventricle muscle activity. Diseases of the mitral valve and the aortic valve lead to a morbidity rate of 44% and 34% respectively [2, 3], if not successfully treated by either repair or replacement with artificial prostheses. Although the pervasiveness of heart valve disease (HVD) is small, in comparison to that of common coronary heart disease, the effect of HVD on human health and medical expenses is disproportionally large. This is due to the expensive treatment costs, medical investigations and the need for long-term follow-up care [4]. Concomitantly, it was reported that the number of patients in need of heart valve replacement was over 280,000 implants worldwide every year [5], and is expected to rise to more than 800,000 annual procedures worldwide by 2050 [6]. However, the replacement of artificial heart valves has been proven to cause a wide variety of valve-related complications, causing sometimes severe disability or even death [7]. One of the main reasons is that hemodynamics induced by artificial heart valves is different from the natural valve. Therefore there is a huge requirement to better quantify the hemodynamic performance of artificial heart valves and to make improvements to the design. Normally, engineering concerns and hemodynamic assessment of prosthetic heart valves include pressure drop, effective orifice area (EOA) and performance index (PI), regurgitation, and

flow patterns and turbulent shear stresses. [3] Fluid mechanics of artificial heart valve has attracted extensive attention in the past, for review papers see Sotiropoulos et al. [8] and Yoganathan et al. [3]. The additional jets, which are generated by mechanical heart valves, usually generate much higher velocity gradients than the natural valve [9]. In addition to the complex core flow, the interaction between the vessel walls and the jets mentioned above is also of great importance. This is due to a high-velocity gradient being formed in the region impacted by the jets, thus generating a high magnitude of wall-shear stress (WSS). This provides a connection between the fluid mechanics of the heart valves and biology of the vessel walls. It is thought that oscillating shear forces plus large WSS gradients promote the development of intimal hyperplasia (IH) [10]. Moreover, a high WSS could lead to stress-related damage to the vessel's endothelial cells [11, 12]. Besides, an aortic aneurysm rupture is believed to occur when the mechanical stress acting on the wall, composed of pressure forces and the WSS, exceeds the strength of the wall tissue [13]. It has also been reported that vessel segments under the impact of low WSS or highly oscillatory WSS are at the highest risk to develop atherosclerosis. Therefore, it is expected that WSS mapping could contribute to the multidisciplinary and multifactorial approach to detect early atherosclerosis [14].

It is obvious that the valve prosthesis requires to be qualified not only from a hydraulics viewpoint but also by including their impact onto the vessel walls into the design and qualification process. Although it has been reported that the oscillation, low or high magnitude of the WSS can lead to severe heart diseases [11, 12], to our knowledge, most

of the previous studies [1, 9, 15] on the qualification of the artificial valves mainly focus on the flow field in the vicinity of artificial valves in simplified straight vessel models. Limited attention has been paid to the effects of the implanted artificial heart valves on WSS magnitude and distribution along the aortic wall [16]. As for measurement methods, there are quite a lot of limitations in performing measurements in a natural condition, as the test section are organs in vivo and the fluid is blood. The limited spatial resolution of the in-vivo measurements such as magnetic resonance imaging (MRI) [17] leads to a challenge to measure WSS accurately. In-vitro measurements such as Particle Image Velocimetry (PIV) still require optical access. It is also difficult to apply direct measurements to such studies by using MEMS sensors. In this study, we applied micro-pillar wall shear stress sensors [18] at the wall along the AAo. In-situ calibration is done herein with highly resolved micro-PIV measurements in a reference flow configuration using an open orifice nozzle.

## 2. Materials and Methods

### Heart valve prosthesis

Artificial heart valves are divided into two major types, mechanical heart valves (MHVs) and bioprosthetic heart valves. [3] It was reported that 20% are with MHVs and 80% of replacements are with bioprosthetic heart valves. [5] There is a growth in the use of the bioprosthetic heart valve as it can be implanted via a catheter in a minimally invasive aortic operation known as transcatheter aortic valve implantation (TAVI). However, the main limitation of the bioprosthetic valve is the valve durability, which is especially critical

to young patients. Therefore it is normally used to treat older patients, with severe symptomatic aortic stenosis who are deemed to be surgically 'high-risk'. [19] Until recently, heart valve replacement was commonly performed using MHV, which offers life-long durability. [8] The focus of the present work is to provide a comparative study of two MHVs, including the St. Jude Medical (SJM) Regent BMHV (St. Jude Medical Inc., Minnesota, U.S.) and the Lapeyre-Triflo FURTIVA mechanical heart valve (TMHV) (Triflo Medical Inc., Neuchâtel, Switzerland), both with the same diameter $D_A$ = 25 mm (see Fig. 1). The SJM Regent valve is a widely used MHV which was introduced in the market in 1978 and therefore is taken as the control valve in the study. The Lapeyre-Triflo FURTIVA TMHV consists of three leaflets that open to form a central orifice for the blood to flow through and three side orifices jets. Several designs of the this valve have been studied over the years in vitro [20, 21], and its in-vivo performance has also been evaluated in animal trials successfully [22]. As the design more closely resembles the native aortic valves, it is assumed to have a better hemodynamic performance. Note that this valve design differs from the valve used in our previous studies [23], see US patent 6,395,024 B1 [24]. More importantly, the Lapeyre-Triflo FURTIVA has no open windows at the leaflet hinges (see Fig. 1 (b)). An open circular orifice nozzle is also used for performing in-situ calibration of the micro-pillar sensors using micro-PIV measurements (Fig. 1 (c)).

**Experimental setup**

The experimental setup for the current study is similar to the setup in previous studies carried out by the authors [23, 25]. For brevity, a short summary of the experimental arrangement is included herein; a more detailed explanation can be found in the aforementioned studies. The geometry of the model aorta is taken from Vasava et al. [26], who simplified the geometry derived from a three-dimensional reconstruction of a series of two-dimensional slices obtained in vivo using CAT scan imaging on a human aorta by Shahcheraghi et al. [27] (see table 1). Although the geometrical dimensions of the human aorta may slightly vary with age and sex, the comparative effects observed between the BMHV and the Lapeyre-Triflo FURTIVA TMHV should represent the relative differences in a realistic manner. The diameter of the aorta is $D_A$ = 25 mm, and the MHVs are chosen to fit the size accordingly. The 180° curved bend representing the aortic arch with sinuses of Valsalva (SOV) has a planar symmetry plane (crossing the left sinus in the middle), which is used for fabrication of the model and sensor integration. The casting process of the transparent aorta model has been described in detail in our previous study [23]. The outer surface of the kernel was polished to a surface roughness of less than 2 micron, which gives a hydraulically smooth surface to the silicone cast. The final model consists of two symmetric halves made out of silicone (Elastosil RT 601™, refractive index n ≈ 1.43) which are later assembled together, as shown in Fig. 2(b). The sensors are integrated into the model via a 200µm thick sheet made from Polydimethylsiloxane (PDMS) (density $\rho_{PDMS} \approx 1030$ kg·m$^{-3}$, Young's modulus $E \approx 1.24$ MPa), which is clamped between the two

halves. The sheet is manufactured such that it follows the extrados of the Aortic arch and is flush to the wall. The 12 micro-pillar sensors then protrude from this edge into the flow field, as seen in Fig. 2(c). Here the micro-pillars are subject to flow-induced drag forces, which causes their bending relative to the situation when the liquid is at rest. For the conditions given below, the displacement of the pillar tips under bending is then proportional to the WSS.

The transparent aorta model is then placed at the bottom of a transparent container (width/depth: 190 mm, height: 500 mm), and subsequently filled with a glycerine-water solution (58/42 % by mass, density $\rho$ = 1140 kg·m$^{-3}$, dynamic viscosity $\mu$= 5 mPa·s at the temperature of 38°C, refractive index 1.41). The refractive index of the glycerine-water solution has been adjusted close to that of the silicone model such that there is good optical access into the inner of the aorta. A picture of the view onto a millimetre paper behind the model demonstrates the effect of reducing the optical distortion along the curved walls of the model (Fig. 2(d)). Small tracer particles (fluospheres, mean diameter 30 µm, Dantec Dynamics, density $\rho_p$ = 1040 kg·m$^{-3}$) are added to the mixture for the PIV measurements during the sensor calibration and flow studies. The Stokes number for these particles is $Stk = \tau U_P/d_p \approx 0.33 \ll 1$, where the peak inlet velocity ($U_P$=0.95 m/s) is taken as the reference velocity and the characteristic time scale is $\tau = \rho_p\, d_p^2/(18\mu) \approx 10\ \mu s$ [28]. This indicates that particles are able to follow the streamlines closely. It must be noted here that the working fluid in the present study has a Newtonian behaviour which differs from the non-Newtonian behaviour of blood. However, for

vessels with a diameter larger than 1 mm it has been observed that blood behaviour can be approximated as a Newtonian fluid [29, 30]. Saying this, Clauser et al. [31] have compared experiments with a newly developed non-Newtonian PIV plasma with blood-like rheological and coagulation properties compared with the water-glycerine mixture. The viscosity of the water-glycerine used in the present study is similar to the average viscosity of the PIV plasma when the wall shear rate change from 100 $s^{-1}$ to 2000 $s^{-1}$. In the present study, the magnitude of the shear rate is found to be in the range of 2000 $s^{-1}$. As such it can be seen that the viscosity used in the present study is within the presented. Therefore it is concluded that the flow in the large vessel of the aorta with the water-glycerine mixture shows similar behaviour as the blood flow.

The MHVs are mounted at the sinus root, in the centre of the transparent container (see Fig. 3(a)). They are orientated, in both cases, such that the left-most leaflet is facing the left sinus in the plane of symmetry. For the tri-leaflet Lapeyre-Triflo FURTIVA TMHV, all three leaflets then face the three sinus bulbs over the circumference as in case of the natural aortic valve. As the Lapeyre-Triflo FURTIVA TMHV is mimicking the natural valve, other orientations than the leaflets facing the sinuses is not meaningful and not intended for implantation. For the bi-leaflet SJM Regent the right leaflet is out of the plane of the sinuses.

For reference measurements, a thin-walled nozzle with circular orifice (outer diameter 25mm, inner diameter 24.6mm) was inserted into the aorta in the same plane as the MHV, which blocks the region of the SOV and generates a smooth core flow into the aorta.

This configuration is studied at the same physiological flow rate for calibration of the sensors with simultaneous micro-PIV measurements.

An 83mm long nozzle, inlet diameter 40mm converging to an outlet diameter of 25mm, was placed upstream of the MHV. The nozzle is designed such that the flow is conditioned as the fluid flows from the left ventricle to the heart valve. Prior to the nozzle inlet, a pulse flow generator is connected via a straight pipe, which generates an entrance length of 1.4 m. A physiological pulsatile flow is generated with a heart rate of 70 beats per minute and a stroke volume of 80ml. To ensure the physiological conditions of the pressure across the valves, a constant pressure head of 80mmHg is applied to the open exit of the aorta. This is done by creating a cushion of pressurised air in the upper half of the tank above the liquid level.

**High-speed particle image velocimetry**

A continuous wave Argon-Ion laser (Raypower 5000, 5 W power at $\lambda$ = 532 nm, Dantec Dynamics) is used as an illumination source. The output laser beam is approximately 1.5 mm in diameter and is further expanded into a sheet illuminating the symmetry plane of the aorta. Full format recordings of the flow in the AAo are taken with a high-speed camera (Phantom Miro 310, Ametek, 576 × 768 $px^2$ recording at 7200 fps) equipped with a lens (Tokima Macro $f$ = 100mm, F 2.8) giving a field of view of 57.6 x 76.8 $mm^2$ (see Fig. 4(b)). Zoomed-in recordings are carried out by an inverted telescopic lens (Model K2/SC™, Infinity Photo-Optical Company, Boulder, USA), which gives a field of view of

4.0 x 6.4 mm² at 7200 fps. This equipment is used for the calibration of the micro-pillar sensors using simultaneous micro-PIV measurements.

An in-house Matlab code is used in order to post process the micro-pillar tip motion and the flow field recordings. For the PIV recordings, the images are masked within the pillar regions and processed with 2D cross-correlation of successive images to calculate the in-plane velocity fields. Processing is done in small interrogation windows with an iterative grid refinement method giving a final window size of 32 x 32 $px^2$. To illustrate the trajectory patterns of the jets in the flow the finite-time Lyapunov exponent (FTLE) is calculated from the velocity fields (LCS MATLAB Kit Version 1.0, Dabiri Lab, Stanford University), where Lagrangian coherent structures (LCSs) are shown by the largest values in the FTLE field. This method has been reported as an efficient way to diagnose time-evolving patterns in dynamical systems [32]. The calculation is done backwards in time with a time interval of 14 ms for 10 snapshots with an interval of 10 snapshots. Another set of High-speed PIV measurements was carried out on the centre plane of the transparent inlet tube, while the pulse generator running at the test conditions. The axial velocity profile *u(r,t)* across the circular cross-section of the tube was determined from the PIV data, and the flow rate *Q(t)* was then calculated from the integral:

$$Q(t) = \int_0^R u(r,t) \cdot 2\pi \cdot r dr \ , \quad (1)$$

where *R* is the inner radius of the inlet tube at the location of the measured profile.

**Wall shear stress imaging**

The first use of measuring the wall shear stress using flexible micro-pillar sensors is documented in Bruecker et al. [18]. The method presented has been used herein in order to obtain comparative measurements of the wall shear stress downstream of the different heart valve prostheses. The static and dynamic response of these sensors illustrated in Fig. 4(a) is characterized by different pillar shapes and fluids in previous studies [18, 33]. For accurate measurements of the WSS there exist several conditions which need to be fulfilled: [18, 23, 33]

- To avoid the gravitational forces which influence the pillar motion, i.e. the density of the flexible micro-pillar sensor should be of the same order of the density of the working liquid. This is the case for the micro-pillars used in the present study.

- Viscous forces should dominate the drag on the pillar. This is when the local Reynolds-number, characterized by the small scale of the pillar, $Re_{Tip} = \rho U_{Tip} d/\mu$ is *O*(10) or less. This ensures also that no vortex shedding occurs. An estimation with a tip velocity of half of the peak velocity $U_P$ yields a value of $Re_{Tip}$ = 10.

- The height of the micro-pillar should be such that it is in the linear range of the velocity profile near the wall. This is often a compromise between sensitivity and visibility. Therefore, a first-order approximation is often estimated in the form $u(y) = U_{Tip}\, y/l + O(\varepsilon)$ with the characteristic velocity ($U_{Tip}$) taken at the tip of the pillar. This approximation is valid if the pillar height is considerably smaller than the boundary layer thickness. From the open nozzle configuration, the average boundary layer thickness in the total flow cycle

was observed to be approximately 5 mm. Thus the pillar is situated only in the first 20% of the boundary layer. Note that this is a mean measure from the large-scale PIV measurements over the whole cycle and instantaneous values might differ depending on the location and time in the flow cycle.

- Streamwise bending of the pillars is small compared to the length of the pillars. Such that the wall-normal forces are only of second-order influence compared to the wall-parallel shear. Herein the streamwise bending is always observed to be less than 10% of the pillar length.

- The presence of the sensors affects the flow only within a range of 10*d*, which is limited to a region of 1 mm around the sensors.

- The time scale of the sensor response should be small compared to the characteristic time-scale of the flow. An estimation of the smallest time-scales in the aorta can be derived from the Kolmogorov scale [34]. If we assume a typical pressure drop over the MHVs of $\Delta p = 1000\ Pa$ and a flow length $L = D_A$, the dissipation rate per unit of mass can be estimated as:

$$\varepsilon = \frac{\Delta p Q}{\rho V} \approx 6.67\ W \cdot kg^{-1} \approx 6.67\ m^2 \cdot s^{-3} \tag{2}$$

where $Q = U_m \pi D_A^2/4$ is the flow rate and $V = L\pi D_A^2/4$ is the volume of the flow segment. The temporal and spatial Kolmogorov scales are then defined according to [34] by

$$\tau_K = \left(\frac{\nu}{\varepsilon}\right)^{1/2}, \eta_K = \left(\frac{\nu^3}{\varepsilon}\right)^{1/4} \tag{3}$$

respectively, where $\nu = \mu/\rho$ is the kinematic viscosity. Thus, the Kolmogorov scales for the considered aorta flows are estimated to be $\tau_K \approx 0.8\,ms$ and $\eta_K \approx 60\,\mu m$. The response time of the micro-pillars is tested by using a step response experiment. Here a force is applied to one of the pillars and the subsequent motion, of how the micro-pillar returns to its equilibrium state, is recorded. The dynamic response is that of a clamped cantilever beam which is critically damped and is represented by the equations for a damped second order oscillator [33, 35]. The sensor response time is calculated to $\tau_{95} = 5ms$ (the response time is defined as the time required to reach 95% of the final equilibrium position) and the response remains nearly constant up to frequencies of 200Hz. This is sufficient for detecting and observing oscillations in WSS that are induced by coherent flow structures. These coherent flow structures are typically more than one order of magnitude larger, in both spatial and temporal scales, compared to those of the Kolmogorov scales. Previous studies confirmed that the important characteristics of heart valve flows are the dominance of large-scale coherent structures over any random fluctuations due to turbulence [8]. For the micro-pillar sensors applied herein, it is further assumed that only the low-frequency range portion persists within the very near-wall region, which is associated with the near-wall dynamics of the coherent vortex structures [18]. These arguments above show that the response time of the sensors is sufficient to address our research questions.

Based on the above assumptions, the micro-pillar tip bending is directly proportional to the wall shear rate with a constant response for frequencies up to 200 Hz [33, 35]. The

proportionality factor is obtained by the in-situ calibration under the same pulsatile flow conditions in the aortic arch. Where the micro-pillars are recorded simultaneously with micro-PIV measurements, in which the tip's displacement along the wall is calibrated by the wall-normal gradient of the tangential velocity profile at the wall.

The micro-pillars labelled from 1 to 12 are placed uniformly along the outer aortic wall in the AAo (see Fig. 3(b)) in the middle between both model halves. The symmetry plane is where the flow is documented most of the time to be 2D with only weak out-of-plane motion, and is also seen from the original particle recordings where there is a long residence time for the particles in the light-sheet plane. It is expected that in this region, peak values of streamwise WSS will be observed when the side-orifice jets, emanating from the gap between the valve ring and leaflets, impact with the aortic wall. For clarity the results will be focused on two of the twelve micro-pillars, which are situated at key locations. One micro-pillar in the upstream region (labelled as pillar #4) and one in the downstream region (labelled as pillar #11). The tip displacement of the micro-pillar structures is detected with sub-pixel resolution (optical measurement uncertainty <0.1 px, maximum tip displacement 10 px). A second-order low-pass filter with a cut-off frequency of 200 Hz is used to reduce measurement noise above the frequency response of the sensor.

The measured tip displacement relative to the stationary tip position (i.e. when the fluid is at rest), is then used to calculate the wall shear rate using the result of the in-situ calibration carried out in the open circular orifice configuration. A sketch of micro-PIV

data processing is shown in Fig. 4(b). To determine the velocity profile near the wall, a cross-correlation of successive images is performed with a window size of 240 × 64 $px^2$ and 75% overlap. An exemplary snapshot of the near-wall velocity profile is plotted in Fig. 4(c). The slope of the linear curve-fit is then further used as the value of the instantaneous streamwise velocity gradient at the wall, i.e. the wall shear rate. The peak value in the time-series of the micro-PIV measurements is used to determine the proportionality constant, which holds for all other instances in the flow profile. The comparative plots of the wall shear rate distribution over the systolic cycle (see Fig. 4(d)) show that the time-resolved micro-pillar signal coincides well with the result of the micro-PIV measurement. At the end of the systolic cycle, the downstream near-wall flow field is quite complex and often not enough tracer particles remain in the interrogation window. This leads to unreliable micro-PIV data in the later phase of valve closure. Note, that imaging of the WSS distribution can be done simultaneously for 4-8 micro-pillar sensors while for the micro-PIV measurements, very high seeding densities are required to get good PIV results near the wall; which is often not possible due to high levels of laser reflection from the wall and particle migration to the core flow away from strong near-wall velocity gradients. This is why measuring the WSS by using the micro-pillar sensors is a much more suitable alternative for complicated flows, as observed in the present study.

## 3. Results

### Inlet flow condition and leaflet kinematics

The inlet flow profile is shown in Fig. 5(a), with a systolic heartbeat duration of $T_{sys}$=386 ms characterised by an accelerated flow phase from 0 to 0.2$T_{sys}$, then a peak systole phase from 0.2$T_{sys}$ to 0.4$T_{sys}$, followed by a decelerated flow phases from 0.4$T_{sys}$ to 0.9$T_{sys}$, and finally the valve closure phase from 0.9$T_{sys}$ to $T_{sys}$. At the peak of the flow, the peak inlet velocity reaches a value of $U_P$ = 0.95 m·s$^{-1}$. The mean velocity averaged over the complete beat cycle amounts to $U_m$ = 0.19 m·s$^{-1}$. The non-dimensional physical parameters of the flow can be represented by the Reynolds number (Eq. 4), Strouhal number (Eq. 5) and Womersley number (Eq. 6):

$$Re_P = \frac{\rho U_P D_A}{\mu} \tag{4}$$

$$St = \frac{D_A}{2}\frac{f}{(U_P - U_m)} \tag{5}$$

$$\alpha = \frac{D_A}{2}\sqrt{\frac{2\pi f \rho}{\mu}}, \tag{6}$$

Where $f$ is the heart rate. When $f$ is 1.15 Hz (70 BPM), it is obtained that, $Re_P = 5340$, $St = 0.019$ and $\alpha = 16$.

The critical peak Reynolds number is calculated according to [36] based on the measured Strouhal number and Womersley number according to Eq. 7.

$$Re_P^c = 169\alpha^{0.83}St^{-0.27} \tag{7}$$

From which the critical peak Reynolds number can be obtained as: $Re_P^c = 4925$. The supracritical Reynolds number is then found to be, $Re_P - Re_P^c = 415$, which indicates that the flow is unstable [36]. The non-dimensional physical parameters of the present study are similar to those that have been observed in the in-vivo experiment of the healthy aorta performed among 30 volunteers by Stalder et al. [36]. This indicates that the flow conditions used in the present study is representative for the natural flow situation.

The flow measurements are supplemented by instantaneous positions of both leaflets of BMHV and Lapeyre-Triflo FURTIVA TMHV, taken from high-speed recordings of the tip motion of the leaflets. It has been reported by Bruecker [37] et al. that all three leaflets of Lapeyre-Triflo FURTIVA TMHV open and close simultaneously, with less than 20ms difference in closure time . The closure was tested for 20 cycles starting from the same initial boundary conditions (rest). Therefore, one profile is representative for all other leaflets. Comparative results of the leaflet motion measurements are given in Fig. 5(b). The leaflets of Lapeyre-Triflo FURTIVA TMHV reach a maximum opening position at an angle of about 75° after $0.1T_{sys}$, while the leaflets of BMHV reach the maximum angle of 85° at $0.2T_{sys}$. The closure of the BMHV leaflets has been observed to vary depending on the orientation of the leaflets relative to the sinuses, i.e. when the left leaflet is facing the left sinus it closes at $0.8T_{sys}$ whereas the right leaflet starts closing much earlier at $0.6T_{sys}$.

**Flow field**

The velocity field is analysed by comparing the instantaneous out-of-plane vorticity contours, with velocity vectors overlaid, at three different time instances for both the BMHV and Lapeyre-Triflo FURTIVA TMHV (Fig. 6). A similar comparison is carried out in Fig. 7, where the contour is this time showing the finite-time Lyapunov exponent (FTLE) at the same time instances as shown in Fig. 6. Using FTLE makes the jets which emenate from the MHVs clearly visable, where regions of high FTLE indicate the boundary from one of the jets. The development of the boundary layer can also be clearly seen by regions of high vorticity near the wall.

*SJM Regent BHMV.* During the valve opening phase (see Fig. 6(a)), the leaflets' leading edges move from outside towards the centre. A pair of vortices form at the outer edges of the leaflets by shear layer separation, marked as outer starting vortices (OSV) for clarity in Fig. 6(a). Flow separation at the edge of the valve housing causes the anti-clockwise vortex penetrating into the left sinus region, which is the so-called aortic sinus vortex (ASV). These vortices affect the near wall flow in the aorta while they travel further up into the AAo (see Fig. 6(b)). Later, regular rows of discrete vortical structures occur downstream of the leaflets with alternating rotation, resembling the form of von Karman-type vortex streets. These vortical structures have been observed by Dasi et al. [9] in their study of the vortex dynamics of the BMHV and also have been reported by De Tullio et al. [15] in their numerical simulation.

The boundary between fluid entering the aorta and the pre-existing fluid inside the aorta, above the valve, is seen as high FTLE values in the left sinus region in Fig. 7(a) and (d). A wash-out flow driven by the ASV can be observed, and the generation of the left side orifice jet (SOJ) is seen in Fig. 7(b). Downstream of the trailing edge of both leaflets the vortex streets appear in the FTLE, and is represented in Fig. 7(b) as vertical columns with a zig-zag type pattern. At peak systole, Fig. 7(c), the side orifice jet attaches to the left wall of the aorta, indicating that there is an impacting of the SOJ onto the outer aortic wall.

*Lapeyre-Triflo FURTIVA TMHV.* In the opening phase of the Lapeyre-Triflo FURTIVA TMHV, the tips of the leaflet move from the centre towards the sinuses, which causes a different flow field in comparison to the SJM. A leading inner starting vortex (ISV) is followed by an outer starting vortex (OSV) once the left leaflet reaches the maximum opening position. Both vortices are convected downstream and a rather uniform core flow, from the central jet, develops. This uniform core jet flow can be clearly seen in Fig. 6(e-f). The TMHV generates higher vorticity towards the centre of the vessel, with a value of 170 $s^{-1}$ at peak systole. However, higher vorticities are observed along the vessel walls in the BMHV case, where a value of 147 $s^{-1}$ along outer radius wall and -221 $s^{-1}$ along the inner radius wall at peak systole can be observed.

Significantly higher FTLE values are observed in the left sinus region in Fig. 7(d), indicating that there is a stronger wash-out flow compared to BMHV, which is supported by the displacement fluid generated by the outwards rotating leaflet. The separated shear layers at the outer and inner edge of the leaflet are presented by the side orifice jet and central

orifice jet separately. Thereafter, these two jets mix and travel towards the centre of the aorta instead of impacting on the vessel wall at peak systole (see Fig. 7(e) and (f)).

In order to obtain an indication of how chaotic the flow is, the absolute value of the out-of-plane vorticity field is integrated across the entire flow domain and normalised the same quantity obtained with the open orifice nozzle configuration. As this will give a numerical value as to the extra vorticity generated in the flow field from the jets and wakes of the valve-ring and occluders.

The normalized integration for BMHV is $E_{BMHV} = 1.93$ at $0.18T_{sys}$, $E_{BMHV} = 1.49$ at $0.25T_{sys}$ and $E_{BMHV} = 1.45$ at $0.4T_{sys}$ over peak systole phase. Compared to BMHV, the normalized integration for the Lapeyre-Triflo FURTIVA TMHV leads to values of $E_{TMHV} = 1.94$ at $0.18T_{sys}$, $E_{TMHV} = 1.34$ at $0.25T_{sys}$ and $E_{TMHV} = 1.27$ at $0.4T_{sys}$. This indicates that the flow field is more chaotic with the BMHV during the peak systole phase. Note that this is obtained only from a single plane in the flow and therefore the conclusion may not necessarily hold for the entire flow field. Saying this, the plane used herein is the symmetry plane for core flow and the associated shear-layers, therefore is a strong indicative for the entire flow domain.

**Wall shear rate**

As the velocity gradient is used for the calibration of the micro-pillar sensors in the near wall region, the results herein are directly presented in terms of wall shear rate. Comparative profiles of wall shear rate in BMHV, Lapeyre-Triflo FURTIVA TMHV and open circular orifice nozzle configurations are presented for the systolic cycle. The circular

orifice configuration can be regarded as the reference flow case (in the aortic arc) for the MHVs, as long as the physiological flow conditions remain. The profiles of wall shear rate measured by the micro-pillar sensors at the upstream region and downstream region are plotted in Fig. 8(a) and (b), respectively.

During the valve opening phase, the flow acceleration generates a progressive rise of the wall shear rate, this trend is consistent across all configurations. In this early phase, the displacement effect, generated by the opening valves, is similar for all configurations. Here the WSS is mainly influenced by bulk flow movement. The measured profiles in this phase strongly resemble those of the reference flow (i.e. without a valve). Thereafter, BMHV shows a further increase in wall shear rate, which is linked to the stronger wash-out flow as observed from the side orifice jet in in Fig. 7(b). Whereas the TMHV does not observe any increase. At around $0.2T_{sys}$, a drop is seen for both MHVs, which is happening when the counter-clockwise rotating vortex structure of the inner starting vortex is travelling along the sensor position. This temporarily induces a reduction of the near-wall flow velocity.

Shortly thereafter, a significant increase in the wall shear rate appears around the peak systole in BMHV (~$0.3\ T_{sys}$). This is caused by the impact of the strong side orifice jets on the outer aortic wall in the AAo, as seen in Fig. 7(b-c). The peak wall shear rate reaches 2123 $s^{-1}$ for the BMHV while the peak wall shear rate with the Lapeyre-Triflo FURTIVA TMHV configuration is only 910 $s^{-1}$. Which is less than half of the BMHV and of similar magnitude to that of the reference case.

After this peak, the shear rate shows the characteristic waviness of wall shear rate profiles. This waviness is due to the shear-layer roll-up at the region between the core flow and the aortic wall when the global flow starts to decelerate. This waviness is larger in BMHV compared with the Lapeyre-Triflo FURTIVA TMHV, which indicates that the rolling-up of the shear layer along the outer aortic wall in the AAo of BMHV is more intense. This phenomenon is more significant further downstream (see Fig. 8(b)) from $0.35T_{sys}$ to $0.6T_{sys}$. Moreover, the peak wall shear rate of BMHV is 2046 $s^{-1}$, which is still twice the value of the peak wall shear rate of Lapeyre-Triflo FURTIVA TMHV in this region, i.e. 1030 $s^{-1}$.

**4. Discussion and Conclusion**

The detailed experimental results of the flow field generated by BMHV in the aortic arch can be compared to previous studies by Dasi et al. [9] and De Tullio et al. [15] with similar non-dimensional flow parameters and inlet flow profiles. As a more realistic curved geometry of the arch is used in the present study, compared to the straight axisymmetric aorta of Dasi et al. [9]. The left leaflet of BMHV is facing directly the sinus, which delays the closing of the valve due to the ASV. Whereas the two leaflets in the study of Dasi et al. [9] show synchronous motion when closing. The leaflet motion applied in the numerical study performed by De Tullio et al. [15] is consistent with present results, and the structure of the asymmetric flow field [15] also supports our flow field results. This also indicates that the curved geometry of the aortic arch is a very important factor when trying to observe what effect the impacting flow structures have on the aortic walls.

During valve opening, a strong wash-out flow at SOV is observed in Lapeyre-Triflo FURTIVA TMHV. It indicates that, compared to BMHV, Lapeyre-Triflo FURTIVA TMHV has a better performance in assisting blood transportation to coronary arteries, which helps with blood supply to the heart muscle. The vortex street, represented as a 'zig-zag' pattern in Fig. 7(b) and (c), caused by the shedding of the wake from the BMHV leaflets is not observed in Lapeyre-Triflo FURTIVA TMHV configuration. Rather, the latter shows a more homogeneous core flow with less small-scale structures generated in the shear layers. The side orifice jet of BMHV impacts on the outer wall of the AAo, causing peak WSS values with more than two-fold magnitude compared to the reference flow at the same inlet flow profile. In comparison, results show that the impact of orifice jets generated by Lapeyre-Triflo FURTIVA TMHV is much weaker than that in the BMHV. A small first WSS peak appears at the same time for both MHVs and for the reference flow, which is induced by the initial wash-out flow. As the side orifice jet of BMHV propagates earlier into the aorta, than the central orifice jet, the WSS signal shows an early occurrence of the maximum peak than the Lapeyre-Triflo FURTIVA TMHV. In comparison, the peak in Lapeyre-Triflo FURTIVA THMV is caused by the central jet impacting further downstream the aortic wall. This indicates that not only the magnitude of mechanical force but also the impact regions are specific to the different valves designs.

The numerical simulation of the flow in the human aorta by Lantz et al. [38], based on MRI-acquired geometry and flow rate of a subject-specific aorta, show that a natural valve can achieve a similar peak in the wall shear rate (~800 $s^{-1}$) to the open orifice nozzle

configuration (at similar pulsatile flow conditions) presented herein. Also, their comparative study between a rigid aorta and a flexible one using fluid-structure interaction (FSI), showed only small differences in the magnitude of the instantaneous WSS in the AAo. This shows that our WSS measurements provide reliable values although our model neglects flexible walls. When transferring the shear rates into stresses, by multiplying with the dynamic viscosity, the mechanical forces along the aortic wall reach peak stresses of 100 $dyn \cdot cm^{-2}$ for BMHV and less than half of that for Lapeyre-Triflo FURTIVA TMHV. Which is comparable to the reference case where stresses of about 40 $dyn \cdot cm^{-2}$ were observed. These peak shear stresses are still beyond the critical value of 15 $dyn \cdot cm^{-2}$ that induces endothelial quiescence and atheroprotective gene expression profile, which was reported by Malek et al. [39]. Compared to our results, the WSS values reported by Meierhofer et al. [17] obtained by an in-vivo MRI study of the flow in the AAo are about an order of magnitude lower. In general, the spatial resolution of an MRI is approximately 1 mm, which may not be sufficient to capture the steep velocity gradients and the wall position with sufficient accuracy. Therefore the MRI result is assumed to substantially underestimate the true WSS. Though the WSS values might be significantly lower than ours, the comparative effects observed between tricuspid and bicuspid aortic valves should represent the relative differences in a realistic manner. Their results showed a 15% higher WSS in the AAo for patients with bicuspid aortic valve caused by inborn connective tissue disease compared to those with the natural tricuspid aortic valves. They concluded that this increase is correlated with the often-observed dilation of the aorta in

such patients. Transferring this conclusion to our comparative WSS measurements, it indicates that Lapeyre-Triflo FURTIVA TMHV may have the potential to largely reduce mechanical forces on the aortic walls compared to the standard mechanical prostheses with only two leaflets.

The above given results and the conclusions come with some limitations. Firstly, the flow is studied only for a selected representative prosthesis size and flow profile. Additional studies may cover a broader range of prosthesis designs, sizes stroke volume and beat rates to draw a more general conclusion. As for the orientation of the MHVs, the Lapeyre-Triflo FURTIVA TMHV is only tested in its natural orientation with the three occluder facing ideally the three sinuses. Thus, any surgical misalignment is not accounted for. Note that the valve orientation could influence the spatial distribution of wall shear stresses and vortical structures [40]. However, it has been shown in our flow field analysis, that those regions are the most critical for generating high WSS where the side-orifice jets impact with the wall. This is exactly where the sensors are implemented around the aortic arch and why we have chosen the corresponding orientation of the MHVs. Therefore this comparative study manages to sheds further light on the physical understanding of the link between WSS and the flow field induced by the MHVs. Finally, there are also limitations of the sensors regarding the spatial and temporal resolution, which might be of relevance when the flow conditions are changed. This needs further elaboration of the measurement uncertainty including those uncertainties introduced by the PIV measurements, currently used for the in-situ calibration. This is ongoing work in our lab.

In summary, the main focus of our study is the mechanical load imposed by WSS along the vessel wall in the AAo when MHV prostheses are implanted. This study describes new time-resolved WSS measurements with an array of in-situ calibrated sensors distributed along the curved aortic wall and tested for two different valve designs. The results illustrate the importance of the design and the impact of side orifice jets on the WSS peak magnitudes and fluctuations along the aortic wall. A detailed distribution of the WSS magnitudes during the whole systolic cycle are obtained and compared to an undisturbed reference flow situation (open nozzle orifice). The results show that the peaks in the WSS are located within the impact regions of the valve-specific orifice jets and vary largely with differing valve designs.

**Acknowledgments**

This work is sponsored by BAE System and the Royal Academy of Engineering (RCSRF1617\4\11), both jointly funding the position of Professor Christoph Bruecker, which is gratefully acknowledged herein. The German Research Foundation supported the position of MSc Franziska Hegner (DFG 1494/25-1) and MSc Qianhui Li (DFG 1494/32-1), which is also gratefully acknowledged. The authors would also like to express our thanks to the Helmholtz Institute of RWTH Aachen University, Germany, for providing the SJM Regent valve and Didier Lapeyre and Triflo Medical Switzerland Sarl for providing the Lapeyre-Triflo FURTIVA valve used in this project. We also thank the Technical University Bergakademie Freiberg which agreed to transfer the experimental system to City,

University of London for future studies in 2015. Our thanks also extends to Mr Edward Talboys whom helped on grammar corrections.

**Author contributions**

**Qianhui Li:**

- Developing the in-situ calibration method in reference flow;

- Measurements, data acquisition and processing;

- Formal analysis and visualisation;

- Drafting the article.

**Franziska Hegner:**

- Building up the experimental system including the aortic arch model with the integrated micro-pillar structures;

- Contributing to the wordings in a part of the introduction, illustration of the experimental setup, the working conditions of wall shear stress sensors applied in the study with the citation of Hegner and Bruecker [23], and the supracritical *Re*;

- Reviewing the draft and improving grammar correctness;

- The Triflo MHV flow results together with the WSS results from the micro-pillar structures calibrated by ex-situ calibration method and published by Hegner and Bruecker [23] provide a good reference to the present study.

**Christoph H. Bruecker:**

- Stewardship, funding acquisition, resources;

- Conceptualisation and methodology;

- Data and image processing;

- Reviewing and improving the draft.

**Funding**

BAE System

Royal Academy of Engineering (RCSRF1617\4\11)

German Research Foundation (DFG 1494/25-1 and DFG 1494/32-1)

## References

[1] Barannyk, O. a. O., P., 2015, "The influence of the aortic root geometry on flow characteristics of a prosthetic heart valve," J. Biomech. Eng., 137(5), p. 051005.
[2] Iung, B., Baron, G., Butchart, E.G., Delahaye, F., Gohlke-Bärwolf, C., Levang, O.W., Tornos, P., Vanoverschelde, J.L., Vermeer, F., Boersma, E., and Ravaud, P., 2003, "A prospective survey of patients with valvular heart disease in Europe: The Euro Heart Survey on Valvular Heart Disease," Eur. Heart. J., 24(13), pp. 1231-1243.
[3] Yoganathan, A. P., He, Z., and Jones, S. C., 2004, "Fluid mechanics of heart valves," Annu. Rev. Biomed. Eng., 6, pp. 331-362.
[4] Coffey, S., Cairns, B.J. and Iung, B., 2015, "The modern epidemiology of heart valve disease," Heart., pp. heartjnl-2014.
[5] Griffin, B. P., Topol, E. J., Nair, D., and Ashley, K., 2008, Manual of cardiovascular medicine, Lippincott Williams & Wilkins.
[6] Huygens, S. A., Goossens, L.M., van Erkelens, J.A., Takkenberg, J.J. and Rutten-van Mölken, M.P., 2018, "How much does a heart valve implantation cost and what are the health care costs afterwards?," Open heart., 5(1), p. e000672.
[7] Fernandez, J., Laub, G.W., Adkins, M.S., Anderson, W.A., Chen, C., Bailey, B.M., Nealon, L.M. and McGrath, L.B., 1994, "Early and late-phase events after valve replacement with the St. Jude Medical prosthesis in 1200 patients," The Journal of thoracic and cardiovascular surgery, 107(2), pp. 394-407.
[8] Sotiropoulos, F., Trung B. L., and Anvar G., 2016, "Fluid mechanics of heart valves and their replacements.," Annual Review of Fluid Mechanics, 48, pp. 259-283.
[9] Dasi, L. P., Ge, L., Simon, H.A., Sotiropoulos, F. and Yoganathan, A.P., 2007, "Vorticity dynamics of a bileaflet mechanical heart valve in an axisymmetric aorta," Phys. Fluids., 19(6), p. 067105.
[10] Haruguchi, H. a. T., S., 2003, "Intimal hyperplasia and hemodynamic factors in arterial bypass and arteriovenous grafts: a review," J. Artif. Organs., 6(4), pp. 227-235.
[11] Walker, P. G. a. Y., A.P., 1992, "In vitro pulsatile flow hemodynamics of five mechanical aortic heart valve prostheses," Eur. J. Cardio-Thorac., 6(Supplement_1), pp. S113-S123.
[12] Marsden, A. L., Bazilevs, Y., Long, C.C. and Behr, M., 2014, "Recent advances in computational methodology for simulation of mechanical circulatory assist devices," Wires. Syst. Biol. Med., 6(2), pp. 169-188.
[13] Raghavan, M. L., Vorp, D. A., Federle, M. P., Makaroun, M. S. and Webster, M. W., 2000, "Wall stress distribution on three-dimensionally reconstructed models of human abdominal aortic aneurysm," J. Vasc. Surg., 31(4), pp. 760-769.
[14] Shaaban, A. M. a. D., A. J., 2000, "Wall shear stress and early atherosclerosis: a review," Am. J. Roentgenol., 174(6), pp. 1657-1665.
[15] De Tullio, M. D., Cristallo, A., Balaras, E. and Verzicco, R. , 2009, "Direct numerical simulation of the pulsatile flow through an aortic bileaflet mechanical heart valve," J. Fluid. Mech., 622, pp. 259-290.
[16] Arzani, A. a. S., S.C., 2018, "Wall shear stress fixed points in cardiovascular fluid mechanics," J. Biomech.
[17] Meierhofer, C., Schneider, E.P., Lyko, C., Hutter, A., Martinoff, S., Markl, M., Hager, A., Hess, J., Stern, H. and Fratz, S., 2012, "Wall shear stress and flow patterns in the ascending aorta in

patients with bicuspid aortic valves differ significantly from tricuspid aortic valves: a prospective study," Eur. Heart. J-Card. Img., 14(8), pp. 797-804.
[18] Brücker, C., Spatz, J., and Schröder, W., 2005, "Feasability study of wall shear stress imaging using microstructured surfaces with flexible micropillars," Exp. Fluids., 39(2), pp. 464-474.
[19] Zahn, R., Gerckens, U., Grube, E., Linke, A., Sievert, H., Eggebrecht, H., Hambrecht, R., Sack, S., Hauptmann, K. E., and Richardt, G., 2010, "Transcatheter aortic valve implantation: first results from a multi-centre real-world registry," Eur. Heart. J., 32(2), pp. 198-204.
[20] Linde, T., Hamilton, K. F., Navalon, E. C., Schmitz-Rode, T., and Steinseifer, U., 2012, "Aortic root compliance influences hemolysis in mechanical heart valve prostheses: an in-vitro study," The International journal of artificial organs, 35(7), pp. 495-502.
[21] Vennemann, B. M., Rösgen, T., Carrel, T. P., and Obrist, D., 2016, "Time-resolved micro PIV in the pivoting area of the triflo mechanical heart valve," Cardiovascular engineering and technology, 7(3), pp. 210-222.
[22] Gallegos, R. P., Rivard, A. L., Suwan, P. T., Black, S., Bertog, S., Steinseifer, U., Armien, A., Lahti, M., and Bianco, R. W., 2006, "In-vivo experience with the Triflo trileaflet mechanical heart valve," The Journal of heart valve disease, 15(6), pp. 791-799.
[23] Hegner, F., and Brücker, C., "Combined TR-PIV and micro-pillar Wall Shear-Stress imaging in the aortic root," Proc. 18th International Symposium on the Application of Laser and Imaging Techniques to Fluid Mechanics, Lisbon, Portugal, July 4-7,2016
[24] Lapeyre, D., and Steinseifer, U., 2002, "Mechanical heart valve," U.S. Patent., 6,395,024.
[25] Hegner, F., Hess, D., Brücker, C., "Volumetric 3D PIV in heart valve flow," Proc. 11TH Int Symp Particle Image Velocimetry–PIV15 Santa Barbara, California,September 14-16, 2015.
[26] Vasava, P., Jalali, P. and Dabagh, M., 2009, "Computational Study of Pulstile Blood Flow in Aortic Arch: Effect of Blood Pressure," In World Congress on Medical Physics and Biomedical Engineering, September 7-12, 2009, Munich, Germany., pp. 1198-1201.
[27] Shahcheraghi, N., Dwyer, H.A., Cheer, A.Y., Barakat, A.I. and Rutaganira, T., 2002, "Unsteady and three-dimensional simulation of blood flow in the human aortic arch," J. Biomech. Eng., 124(4), pp. 378-387.
[28] Raffel, M., Willert, C. E., Scarano, F., Kähler, C. J., Wereley, S. T., and Kompenhans, J., 2018, Particle image velocimetry: a practical guide, Springer.
[29] Kim, T., Cheer, A.Y. and Dwyer, H.A., 2004, "A simulated dye method for flow visualization with a computational model for blood flow," J. Biomech., 37(8), pp. 1125-1136.
[30] Fung, Y. C., 2013, "Biomechanics: mechanical properties of living tissues," Springer Science & Business Media.
[31] Clauser, J., Knieps, M.S., Büsen, M., Ding, A., Schmitz-Rode, T., Steinseifer, U., Arens, J.and Cattaneo, G. , 2018, "A Novel Plasma-Based Fluid for Particle Image Velocimetry (PIV): In-Vitro Feasibility Study of Flow Diverter Effects in Aneurysm Model," Ann. Biomed. Eng., pp. 1-8.
[32] Haller, G. a. S., T., 2011, "Lagrangian coherent structures and the smallest finite-time Lyapunov exponent. Chaos," An Interdisciplinary Journal of Nonlinear Science., 21(2), p. 023115.
[33] Brücker, C., Bauer, D. and Chaves, H., 2007, "Dynamic response of micro-pillar sensors measuring fluctuating wall-shear-stress," Exp. Fluids., 42(5), pp. 737-749.
[34] Kundu, P. K., Cohen, I.M. and Dowling, D.R., 2012, "Fluid Mechanics."
[35] Dickinson, B. T., Singler, J.R. and Batten, B.A. , 2012, "Mathematical modeling and simulation of biologically inspired hair receptor arrays in laminar unsteady flow separation," J. Fluid. Struct., 29, pp. 1-17.

[36] Stalder, A. F., Frydrychowicz, A., Russe, M. F., Korvink, J. G., Hennig, J., Li, K. and Markl, M., 2011, "Assessment of flow instabilities in the healthy aorta using flow‐sensitive MRI," J. Magn. Reson. Imaging., 33(4), pp. 839-846.
[37] Brücker, C., Steinseifer, U., Schröder, W., and Reul, H., 2002, "Unsteady flow through a new mechanical heart valve prosthesis analysed by digital particle image velocimetry," Meas. Sci. Technol., 13(7), p. 1043.
[38] Lantz, J., Renner, J. and Karlsson, M., 2011, "Wall shear stress in a subject specific human aorta—influence of fluid-structure interaction," Int. J. Appl. Mech., 3(04), pp. 759-778.
[39] Malek, A. M., Alper, S. L., and Izumo, S., 1999, "Hemodynamic shear stress and its role in atherosclerosis," Jama, 282(21), pp. 2035-2042.
[40] Gülan, U., and Holzner, M., 2018, "The influence of bileaflet prosthetic aortic valve orientation on the blood flow patterns in the ascending aorta," Medical engineering & physics, 60, pp. 61-69.

## Figure Captions List

Fig. 1 (a) SJM Regent BMHV, with the leaflets in a fully open position (opening angle: 85°) and in the closed position (closed angle 25°). (b) Lapeyre-Triflo FURTIVA TMHV, with the leaflets in the fully open position (opening angle 75°) and in the closed position (closed angle 40°). (c) Thin-walled nozzle with the circular orifice. The solid arrow marks the centre orifice jet, and the dashed arrow marks the side orifice jet.

Fig. 2 Transparent silicone model of the aorta with the components to manufacture the model such as (a) the kernel of the aorta and (b) the final model assembled by the two symmetric halves. The foil with the pillars sketched in (c) is clamped between both halves. (d) Side view of the fluid basin with a millimetre paper at the back to demonstrate the refractive index matching.

Fig. 3 (a) Top view of the experimental setup. (b) Frontal view of the measurement regions in the centre plane. Full AAo (the black rectangle downstream of MHV): 46x73.7 $mm^2$. Zoom-in region (red rectangle): 4.0 x 6.4 $mm^2$. Inlet flow measurement region (the black rectangle upstream of MHV): 25 x 11 $mm^2$. PDMS sheet with micro-pillars is shown in black. Picture b) changed after Hegner and Bruecker [19].

Fig. 4 (a) Parameters and the working principle of the micro-pillar sensors. (b) The sketch of the micro-PIV data processing. The domain of image processing is denoted by the dashed blue box, in which the image processing windows distribute along *y*-direction with 75% overlap (the first window is denoted by the red box). (c) Plots of near wall velocity measured by the micro-PIV (blue crosses) and linear curve-fitting. (d) Plots of the wall shear rate over the systolic cycle in reference flow situation.

Fig. 5 (a) Inlet flow profile measured from high-speed PIV in the inlet tube and calculated using eq. (1), where $Q_{sys}$ is the peak flow rate over the systolic cycle. (b) Profile of the motion of the leaflet's angular position over the systolic cycle.

Fig. 6 Color-coded distribution of the out-of-plane component of the vorticity overlaid on snapshot vector fields at (a)(d) t/Tsys = 0.1, (b)(e) t/Tsys = 0.18, (c)(f) t/Tsys = 0.25. OSV marks outer side (near the SOV) starting vortex. ISV marks inner side (near the centreline) starting vortex.

Fig. 7 Evolution of jet trajectories illustrated by the colored FTLE overlaid on snapshot vector fields at (a)(d) $t/T_{sys}$ = 0.1, (b)(e) $t/T_{sys}$ = 0.18, (c)(f) $t/T_{sys}$ = 0.25. SOJ marks side orifice jet. COJ marks centre orifice jet.

Fig. 8 Plots of wall shear rate on (a) upstream region and (b) downstream region of the outer wall of the AAo over the systolic cycle. Black dash-dotted line:

open circular orifice nozzle, red dashed line: SJM Regent BMHV, blue line: Lapeyre-Triflo FURTIVA TMHV.

## Table Caption List

Table 1 Main geometry data of the aorta model, taken from Vasava et al. [26], see also [25].

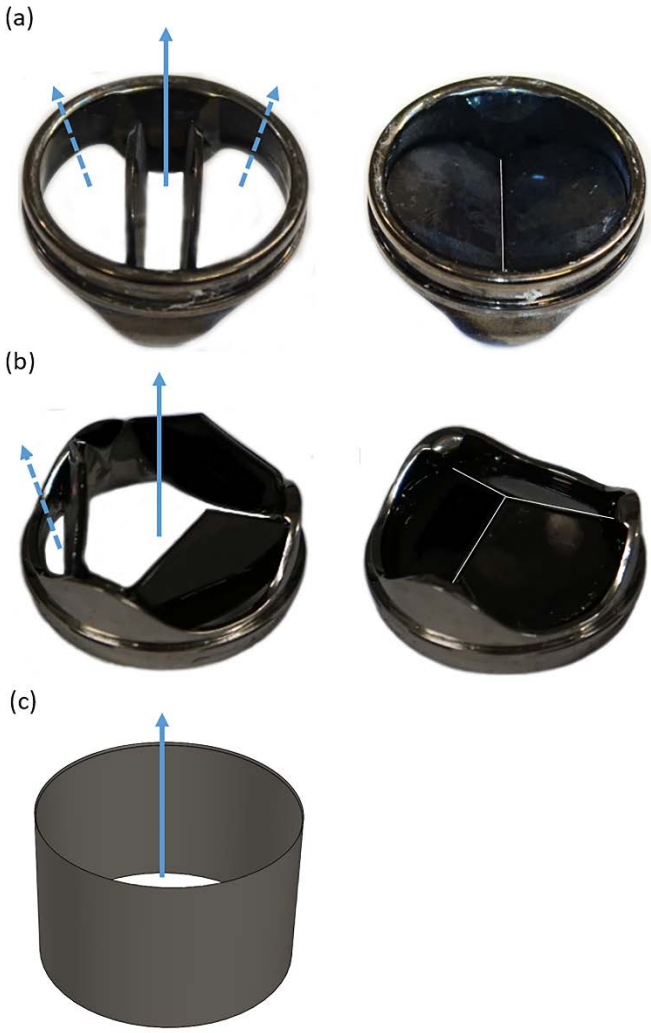


**Fig. 1.** (a) SJM Regent BMHV, with the leaflets in a fully open position (opening angle: 85°) and in the closed position (closed angle 25°). (b) Lapeyre-Triflo FURTIVA TMHV, with the leaflets in the fully open position (opening angle 75°) and in the closed position (closed angle 40°). (c) Thin-walled nozzle with the circular orifice. The solid arrow marks the centre orifice jet, and the dashed arrow marks the side orifice jet.

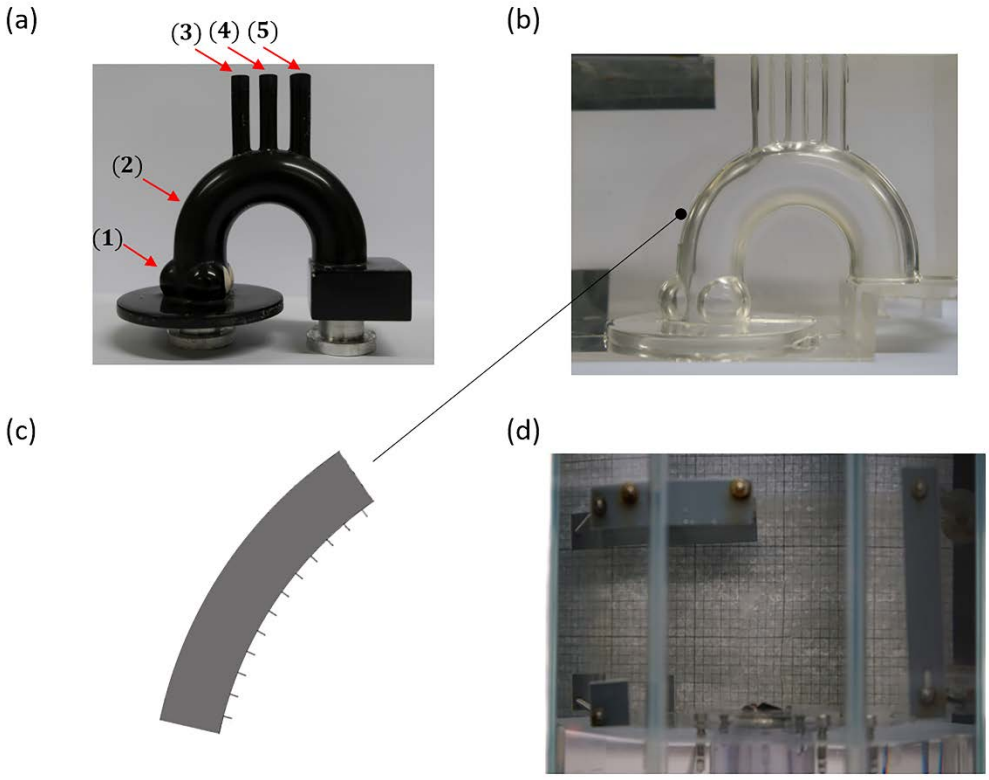


**Fig. 2.** Transparent silicone model of the aorta with the components to manufacture the model such as (a) the kernel of the aorta and (b) the final model assembled by the two symmetric halves. The foil with the pillars sketched in (c) is clamped between both halves. (d) Side view of the fluid basin with a millimetre paper at the back to demonstrate the refractive index matching.

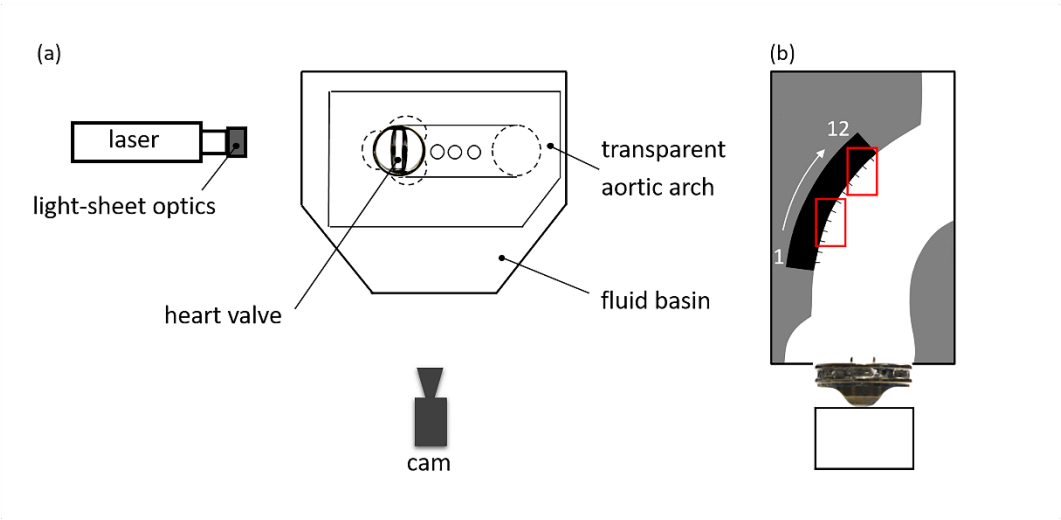


**Fig. 3.** (a) Top view of the experimental setup. (b) Frontal view of the measurement regions in the centre plane. Full AAo (the black rectangle downstream of MHV): 46x73.7 mm². Zoom-in region (red rectangle): 4.0 x 6.4 mm². Inlet flow measurement region (the black rectangle upstream of MHV): 25 x 11 mm². PDMS sheet with micro-pillars is shown in black. Picture b) changed after Hegner and Bruecker [23].

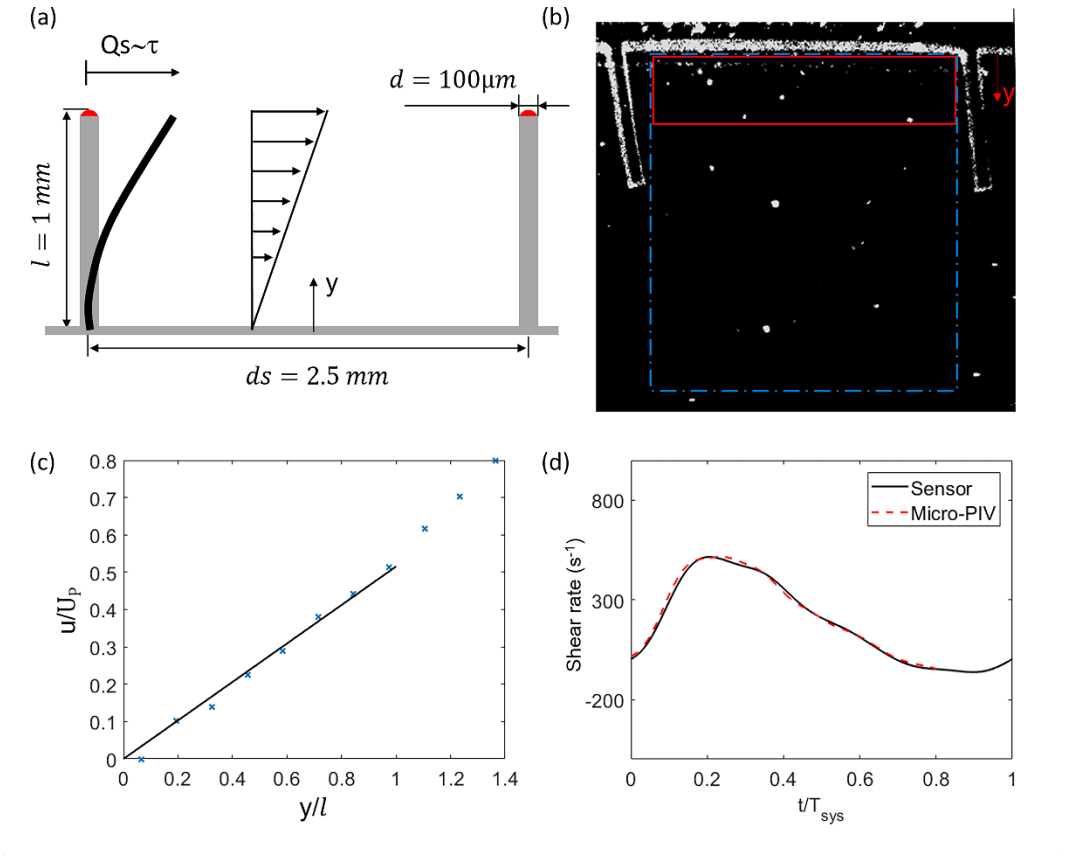


**Fig. 4.** (a) Parameters and the working principle of the micro-pillar sensors. (b) The sketch of the micro-PIV data processing. The domain of image processing is denoted by the dashed blue box, in which the image processing windows distributes along *y*-direction with 75% overlap (the first window is denoted by the red box). (c) Plots of near wall velocity measured by the micro-PIV (blue crosses) and linear curve-fitting. (d) Plots of the wall shear rate over the systolic cycle in reference flow situation.

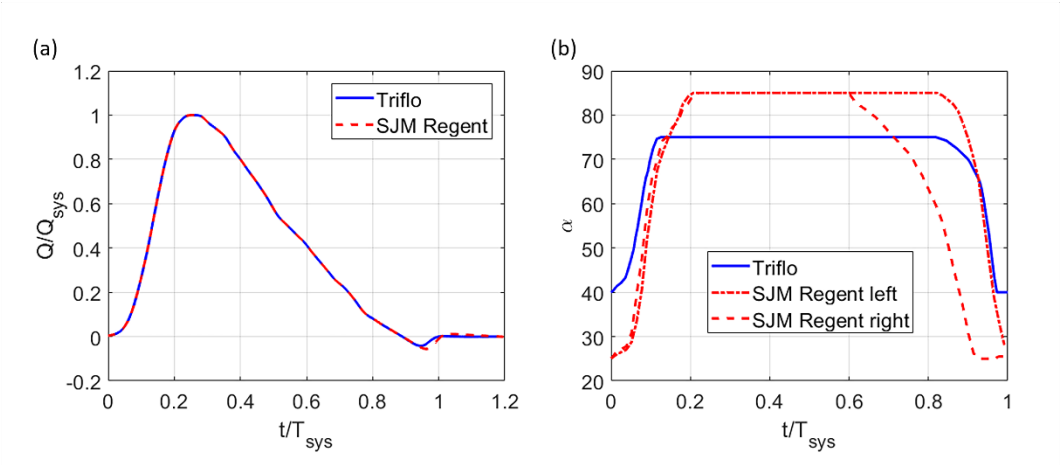


**Fig. 5.** (a) Inlet flow profile measured from high-speed PIV in the inlet tube and calculated using eq. (1), where $Q_{sys}$ is the peak flow rate over the systolic cycle. (b) Profile of the motion of the leaflet's angular position over the systolic cycle.

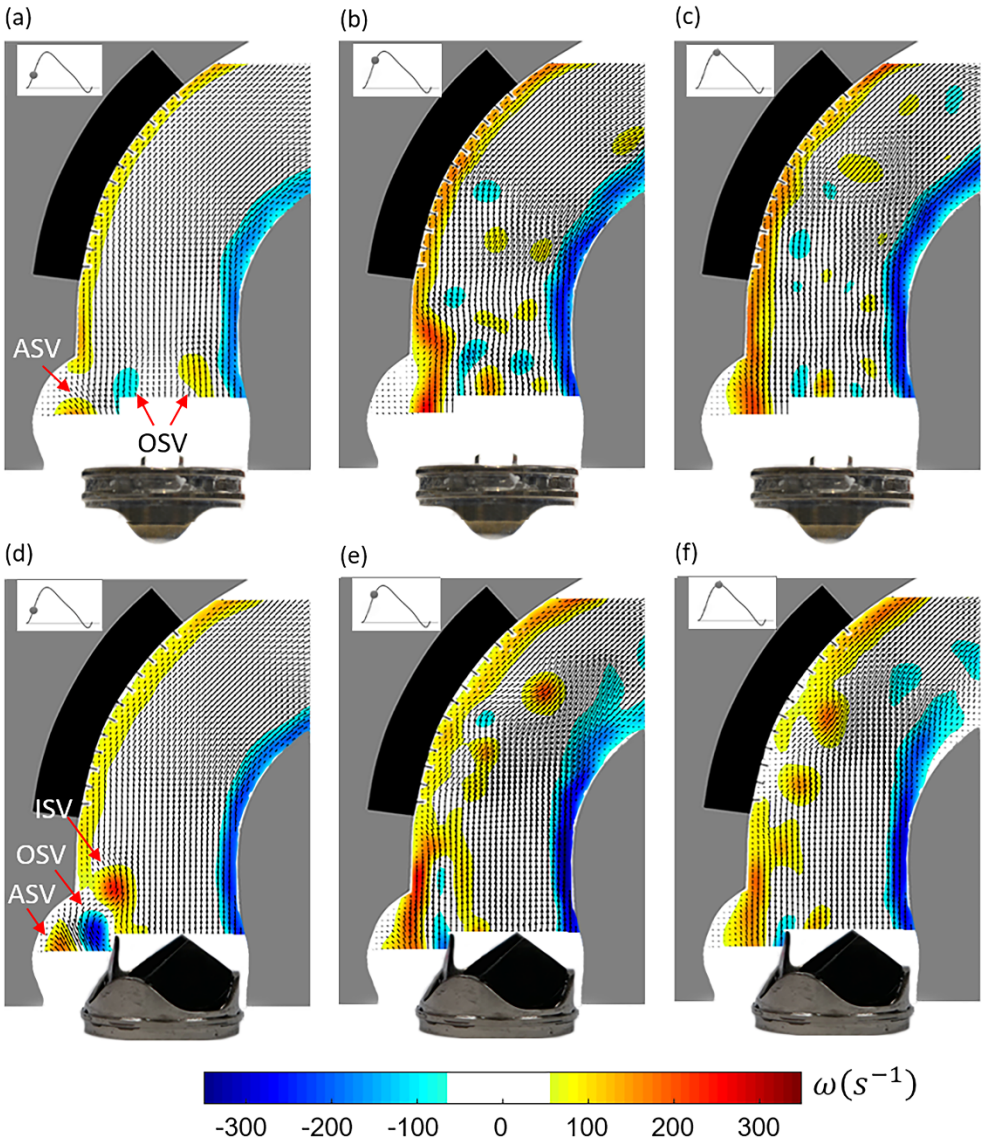


**Fig. 6.** Colour-coded distribution of the out-of-plane component of the vorticity overlaid on snapshot vector fields at (a)(d) $t/T_{sys}$ = 0.1, (b)(e) $t/T_{sys}$ = 0.18, (c)(f) $t/T_{sys}$ = 0.25. OSV marks outer side (near the SOV) starting vortex. ISV marks inner side (near the centreline) starting vortex.

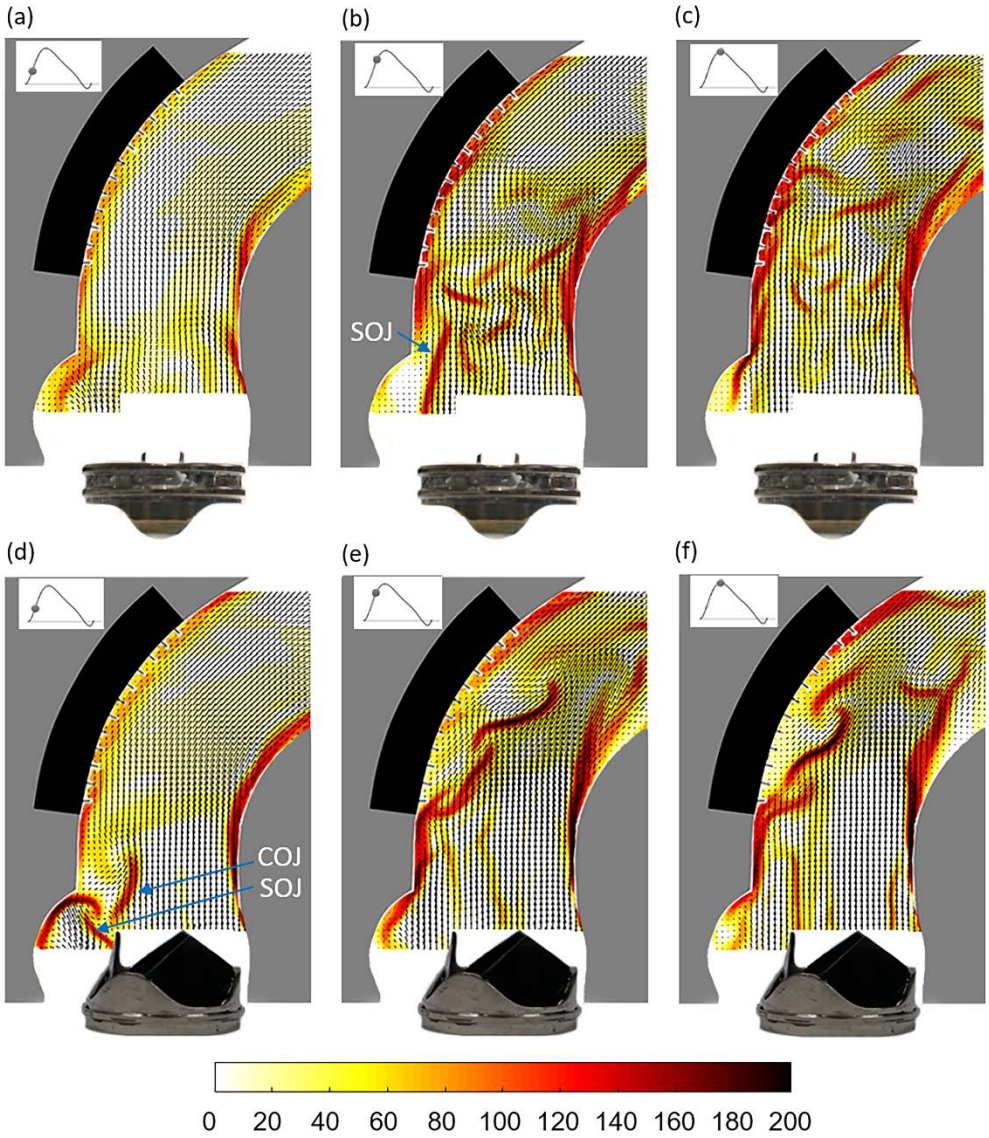


**Fig. 7.** Evolution of jet trajectories illustrated by the coloured FTLE overlaid on snapshot vector fields at (a)(d) $t/T_{sys}$ = 0.1, (b)(e) $t/T_{sys}$ = 0.18, (c)(f) $t/T_{sys}$ = 0.25. SOJ marks side orifice jet. COJ marks centre orifice jet.

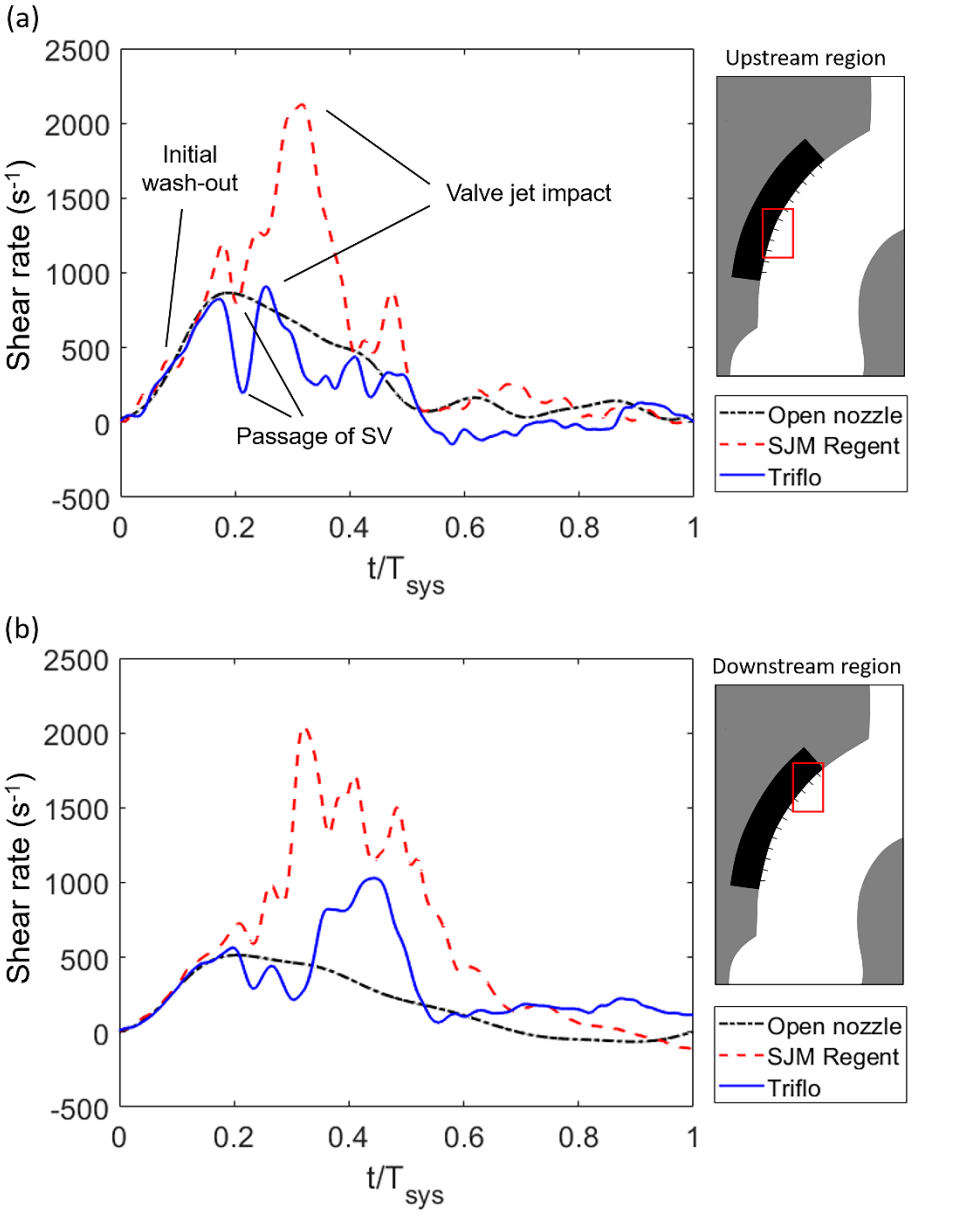


**Fig. 8.** Plots of wall shear rate on (a) upstream region and (b) downstream region of the outer wall of the AAo over the systolic cycle. Black dash-dotted line: open circular orifice nozzle, red dashed line: SJM Regent BMHV, blue line: Lapeyre-Triflo FURTIVA TMHV.

| Artery properties | Dimension (mm) |
|---|---|
| (1) Diameter of sinus bulb | 21 |
| (2) Lumen diameter of ascending and descending aorta | 25 |
| (3) Lumen diameter of brachiocephalic artery (BA) | 8.8 |
| (4) Lumen diameter of left common carotid artery (LCA) | 8.5 |
| (5) Lumen diameter of left subclavian artery (LSA) | 9.9 |

**Table 1.** Main geometry data of the aorta model, taken from Vasava et al. [26], see also [25].